SAND2020-0949C
Proceedings of the ASME 2020
14th International Conference on Energy and Sustainability
ES2020
June 8-10, 2020, Denver, CO, USA

ES2020-6384

# PAIRING DIRECTIONAL SOLAR INPUTS FROM RAY TRACING TO SOLAR RECEIVER/REACTOR HEAT TRANSFER MODELS ON UNSTRUCTURED MESHES: DEVELOPMENT AND CASE STUDIES

**H. Evan Bush, Andrew J. Schrader, Peter G. Loutzenhiser**

G. W. W. School of Mechanical Engineering, Georgia Institute of Technology, Atlanta, Georgia, USA

## ABSTRACT

*A novel method for pairing surface irradiation and volumetric absorption from ray tracing to computational heat transfer models is presented. The method is well-suited to directionally and spatially-complex concentrated radiative inputs, such as in solar receivers and reactors. The method employs a generalized algorithm for directly mapping absorbed rays from the ray tracing model to boundary or volumetric source terms in the computational mesh. The algorithm is compatible with unstructured, two and three-dimensional meshes with varying element shapes. To validate the method, four case studies were performed on a directly irradiated, windowed solar thermochemical reactor model. The method was shown to be energy conservative and to preserve spatial variation when mapping rays from a Monte Carlo ray tracing model to the computational heat transfer model in ANSYS Fluent.*

Keywords: concentrating solar, solar receiver/reactor, directly-irradiated, radiation, CFD, ray tracing, ANSYS Fluent

## NOMENCLATURE

| | |
|---|---|
| $a, b, c$ | barycentric coordinate locations |
| $A$ | area |
| $E$ | thermal energy |
| $H$ | irradiation |
| $k$ | thermal conductivity |
| $n$ | integer number |
| $N_{rays}$ | total number of rays in ray tracing model |
| $M$ | integer number |
| $q$ | heat rate |
| $Q$ | thermal energy |
| $r$ | position vector |
| $S$ | set |
| $t$ | boundary thickness, barycentric coordinate |
| $T$ | temperature |
| $V$ | volume, integer number of face/cell vertices |
| $\vec{V}$ | velocity vector |
| $U$ | heat transfer coefficient |
| $\bar{X}$ | mesh face/cell vertex location vector |

### Greek Letters

| | |
|---|---|
| $\alpha$ | total, hemispherical surface absorptance |
| $\kappa$ | linear absorption coefficient |
| $\rho$ | density |

### Subscripts

| | |
|---|---|
| $\infty$ | environment conditions |
| 1, 2, 3 | triangle/tetrahedron edges and coordinates |
| i | face index |
| k | ray index |
| local | local barycentric coordinate system |
| n | normal direction |
| N | nearest neighbor |
| nb | neighboring fluid cell |
| P | energy loss/error, MCRT grid to CFD mesh |
| R | radiation |
| s | surface |
| sun | real or simulated concentrated sunlight |

### Superscripts/Accents

| | |
|---|---|
| “ | value per unit area, e.g. boundary flux |
| ‘ | value per unit volume, e.g. volumetric source |
| ^ | unit vector |
| . | time rate of change |

### Abbreviations

| | |
|---|---|
| 2D, 3D | two, three dimensional |
| CFD | computational fluid dynamics |
| FV-RTE | finite volume radiative transport equation |
| HFSS | high-flux solar simulator |
| MCRT | Monte Carlo ray tracing |
| SSE | summed square of errors |
| STInGR | Solar Thermochemical Inclined Granular Flow Reactor |
| UDF | user-defined function |




Sandia National Laboratories is a multimission laboratory managed and operated by National Technology & Engineering Solutions of Sandia, LLC, a wholly owned subsidiary of Honeywell International Inc., for the U.S. Department of Energy’s National Nuclear Security Administration under contract DE-NA0003525.

## 1. INTRODUCTION

Detailed computational modeling is used to evaluate and optimize the designs of solar receivers/reactors. Simultaneous capture of heat transfer, fluid dynamics, radiative exchange, and chemical reaction phenomena is well documented [1, 2] and supported by commercial computational fluid dynamics (CFD) software [3]. Concentrating solar processes, though, employ intense, directional radiative inputs, which introduce unique and less-documented modeling challenges. Currently, modeling a solar input may require manual, approximate definitions of complex radiative boundary conditions or extension of the computational domain to include concentrating infrastructure. Either route may reduce model accuracy and/or increase model complexity. An alternative, algorithmically-simple method is presented for direct mapping from Monte Carlo ray tracing (MCRT) to finite volume approximations to the energy and radiative transport equations (FV–RTE).

MCRT and FV–RTE are two methods for modeling solar inputs in receiver/reactor models. MCRT is a statistical method to predict radiative absorption by surfaces and participating media with specified radiative properties [4]. Challenges in implementing MCRT for solar receivers/reactors occur when modeling optically thick media, wavelength/temperature-dependent radiative properties, and complex geometries. These conditions challenges are more tractable with FV–RTE methods and the similar discrete ordinates (DO) method, which are supported in computational software [5]. FV-RTE methods are computationally expensive for domains requiring high mesh resolutions, like combined models of solar receivers/reactors and collecting/generating infrastructure. Fortunately, MCRT and FV-RTE methods have complementary strengths. MCRT may be used to model the concentrated solar input to the receiver/reactor, and FV-RTE may be used to capture internal radiative transport within the reactor. If paired appropriately, the models are a powerful tool for modeling radiative heat transfer to and within solar receivers/reactors.

Prior methods for pairing MCRT and FV-RTE have been implemented by employing 1) non-overlapping or 2) overlapping domains. In non-overlapping schemes [6-9], models of the solar input are mapped to the CFD model at a common boundary through an intensive process of translating directional solar inputs to intensity boundary conditions. Non-overlapping schemes are often necessary in designs with falling/entrained solid particles which participate in the radiative exchange [9]. Non-overlapping schemes may be functionally energy-conservative. However, fine meshes, directionally aligned with the solar input, are required to mitigate discretization error, which may extend computation time and inhibit convergence. As a result, restricting non-overlapping schemes to 2D domains has been recommended [7].

In overlapping schemes [10-14] portions of the MCRT and CFD modeling domains are spatially coincident. In these schemes, the external radiative input is modeled from the collector/generator until it is 1) absorbed by internal receiver/reactor surfaces or media; or 2) rejected from the receiver/reactor by reflection, transmission, or scattering. Absorbed input irradiation is input to the CFD model as a boundary or volumetric source. Re-emission within the receiver/reactor is captured separately, within the CFD model. For diffuse surfaces, overlapping schemes permit coarser CFD meshes that are not required to be directionally aligned with the solar input. Errors result during CFD discretization from representing curved geometries in the MCRT domain as planar approximations in the CFD domain [14], but are mitigated by control of the mesh resolution.

Absorbed rays in overlapping schemes have been implemented as constant surface [15] or sub-surface [16, 17] averaged fluxes. These approximations maintained energy conservation but reduced spatial accuracy between the MCRT and CFD domains. Alternatively, absorbed rays have been binned within a gridded MCRT modeling domain to produce a spatial irradiation profile and interpolated to the CFD mesh [10]. This approximation maintained spatial accuracy for sufficiently fine grids but did not guarantee energy conservation.

The proposed direct mapping method for MCRT–CFD introduces no spatial or energy conservation errors beyond the MCRT precision and CFD mesh resolution. The method is compatible with 2D and 3D domains, structured and unstructured meshes, commercial and in-house ray tracing and CFD models, and surfaces of any shape and orientation. The method is demonstrated in ANSYS Fluent via user-defined functions (UDFs) written in the C programming language. Method validation is performed for a cavity-type solar thermochemical reactor with direct radiative input from a seven-lamp high flux solar simulator (HFSS). Implementation directions for ANSYS Fluent v19.0 and example UDF source codes written in C are available in Appendices A and B of [18].

## 2. METHODS

Monte Carlo ray tracing allows the directional modeling of radiative heat transfer by partitioning a radiation source such as concentrating solar collectors (*e.g.* heliostats, parabolic troughs/dishes) or generators (*e.g.* high flux solar simulators; HFSS), into rays or individual packets of energy, represented as:

$$\dot{E}_{\mathrm{k}} = \frac{\dot{Q}_{\mathrm{sun}}}{N_{\mathrm{rays}}} \tag{1}$$

where $\dot{Q}_{\mathrm{sun}}$ is the radiative power, here evenly partitioned among $N$ rays. $N_{\mathrm{rays}}$ is typically between $10^5$ and $10^7$, with convergence expected for $N_{\mathrm{rays}} \to \infty$. The path of a given ray $k = 1, 2, \ldots, N_{\mathrm{rays}}$ is defined via [4]:

$$\vec{r}_{\mathrm{k}} = \vec{r}_{0,\mathrm{k}} + D\hat{s}_{\mathrm{k}} \tag{2}$$

where $\vec{r}_{\mathrm{k}}$ is the ray intersection, located a distance $D$ and direction $\hat{s}_{\mathrm{k}}$ from the ray origin $\vec{r}_{0,\mathrm{k}}$, *i.e.* the location of ray generation (introduction to the model) or previous ray interaction (*e.g.* reflection, scattering). Ray origin and interaction characteristics are defined stochastically from domain radiative properties.

### 2.1 Irradiated Surface Mapping

A point mapping algorithm is applied to ray intersections to translate absorbed irradiation from a MCRT model to boundary sources in a computational fluid dynamics (CFD) model. The mapping for a group of $\vec{r}_k$, depicted as red points, is given in Figure 1 for a solar reactor aperture and cavity. A detail view shows the mapping for two $\vec{r}_k$ on a single mesh face $F_i$ of the CFD model. The $\vec{r}_k$ are transformed to a local, barycentric coordinate system $(\hat{t}_1, \hat{t}_2)$ on $F_i$ to determine whether they fall within the boundaries of, and are to be mapped to, $F_i$. The process is repeated until each of the $\vec{r}_k$ are sorted into a $F_i$.

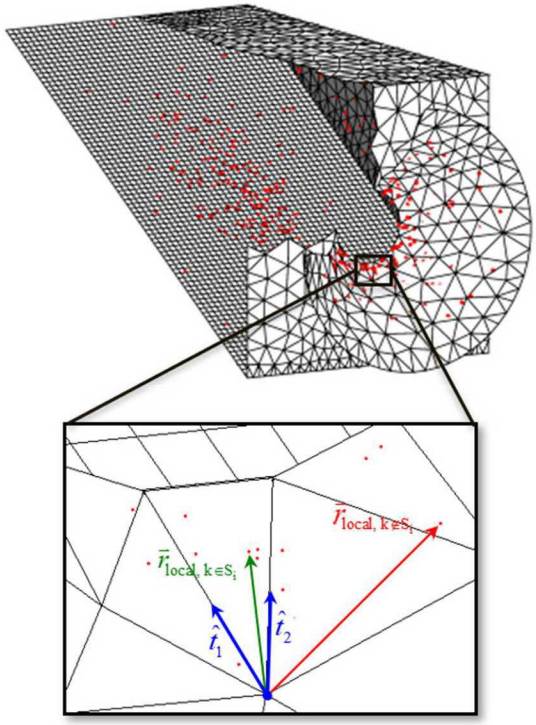


**Figure 1.** Monte Carlo ray tracing intersections (red points) on the surfaces of a solar reactor (left) overlaid on the computational mesh (black lines) to which the rays are coupled; and (right) a detail view of a mesh face on the reactor aperture with unit vectors of the local coordinate system (blue) for ray mapping, as well as the position vectors of two ray intersections: one within the mesh face (green) and one not (red).

For triangular $F_i$, the local coordinate system origin is defined at any of the three $F_i$ vertices, where the basis vectors $t_1$ and $t_2$ are in the directions from the origin to each of the two remaining $F_i$ vertices, respectively. For quadrilateral or greater $F_i$, the face is first subdivided into multiple triangular subcomponents which are each tested. The two-dimensional, local intersection position vectors are defined as:

$$\vec{r}_{local} = at_1 + bt_2 \tag{3}$$

where $(a,b)$ are the local coordinate dimensions. The subset of rays falling within $F_i$ is defined by:

$$S_i = \left\{ k = 1,2,\ldots,N_{rays} \;\middle|\; \begin{matrix} a_{i,k},\, b_{i,k} > 0, \\ a_{i,k} + b_{i,k} \le 1 \end{matrix} \right\} \tag{4}$$

The direct mapping method is depicted in Figure 1 for two example intersections at the given $F_i$, where one intersection (green vector) falls within and one (red vector) falls outside $F_i$.

CFD model boundary sources for each $F_i$ are computed from mapped, summed ray energies as:

$$q''_{sun,i} = (\alpha H_0)_{sun,i} = \frac{1}{A_{s,i}} \sum_{k \in S_i} \dot{E}_k \tag{5}$$

where $(\alpha H_0)_{sun}$ is the absorbed component of the surface irradiation profile $H_{0,sun}$ and $A_s$ is the face surface area. The summation is limited only to the rays within the subset $S$. The boundary sources are incorporated into a general surface-fluid mixed boundary condition to the heat diffusion equation as:

$$-k_{n,i} \left.\frac{\partial T}{\partial n}\right|_{s,i} + q''_{sun,i} = U_i \left(T_{s,i} - T_{\infty,i}\right) + q''_{R,i} \tag{6}$$

where the first term on the left-hand side is the conductive heat flux in the direction normal to the surface $n$ and the first and second terms on the right-hand side are the convective and radiative heat fluxes, respectively. The convective heat flux uses an overall heat transfer coefficient $U$ to account for contact resistance and/or thin-wall conduction. The net radiative heat flux $q''_R$ resulting from the internal radiative exchange is computed via the FV-RTE.

### 2.2 Participating Volumetric Cell Mapping

MCRT has been employed to model heat transfer of radiatively participating media in solar receivers/reactors with quartz windows [19-22], reticulated porous ceramics/metal foams [23-26], and particulates [27-30]. Participating media attenuates directional input radiation by absorption and scattering within the modeled medium, augmenting the resultant surface heat fluxes. The $D$ and $\hat{s}_k$ defining a given $\vec{r}_k$ are additionally dependent upon absorption, scattering, and interface refraction.

Volumetrically absorbed rays are mapped into the discretized volumetric domain by a similar algorithm to surface mapping: globally-defined points of absorption $\vec{r}_k$ are transformed into a local, barycentric coordinate system $(t_1, t_2, t_3)$ based on the tetrahedral element $C_i$. For more complex element shapes, the $C_i$ is first subdivided into $M$ tetrahedral sub-elements which are each tested. Subdivision of a given element $C_i$ and volumetric mapping of two $\vec{r}_k$, depicted as red points, are shown in Figure 2, where the transparent surface bounds a sub-element.

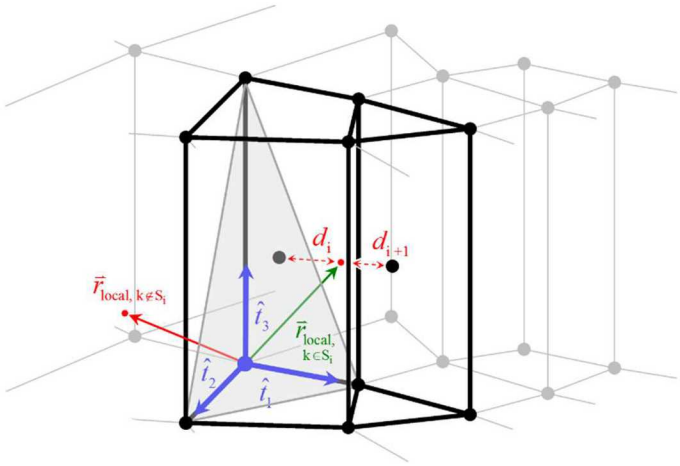


**Figure 2.** Monte Carlo ray tracing intersections (red points) within a discretized computational mesh (gray wireframe) to which the rays are coupled, with: 1) unit vectors of the local coordinate system (blue) for a tetrahedral region (transparent gray surface) of a given cell (black lines); 2) position vectors of two ray intersections within the cell (green arrow) and outside the cell (solid red arrow); and 3) straight-line distances (dashed red arrows) from one absorbed ray to the centroids of the cell $i$ and a neighbor $i$ + 1 (black wireframe).

The three-dimensional, local absorption point position vectors are defined as:

$$\vec{r}_{\text{local}} = at_1 + bt_2 + ct_3 \tag{7}$$

where ($a$,$b$,$c$) are the local coordinates. The subset of rays that fall within $C_i$ is defined by:

$$S_i = \left\{ k = 1,2,\ldots,N \,\middle|\, \begin{matrix} a_{i,k},\, b_{i,k},\, c_{i,k} > 0, \\ a_{i,k} + b_{i,k} + c_{i,k} \le 1 \end{matrix} \right\} \tag{8}$$

The direct mapping method is depicted in Figure 2 for two example intersections at the given $C_i$, where one intersection (green vector) falls within $C_i$ and one (red vector) falls outside.

Volumetric sources for each $C_i$ are computed from mapped, summed ray energies as:

$$\dot{q}'''_{\text{sun,i}} = \left( \kappa \int_{4\pi} I(s')\, d\Omega' \right)_{\text{sun,i}} = \frac{1}{V_i} \sum_{k \in S_i} \dot{E}_k \tag{9}$$

where $\kappa \int_{4\pi} I(\vec{s}')\, d\Omega'$ is the absorbed component of the entering radiation from all directions $\vec{s}'$ and over all solid angles Ω' for a linear absorption coefficient $\kappa$; and $V$ is the cell volume. The summation is limited only to the rays within the subset $S$. The volumetric heat sources are applied at each $C_i$ as a term in the thermal energy transport equation, a common form of which is represented as:

$$\frac{\partial E_i}{\partial t} + \nabla \cdot \left( \rho \vec{V} h \right)_{\text{nb,i}} = \nabla \cdot \left( k \nabla T_i \right) + q'''_{\text{sun,i}} + q'''_{\text{R,i}} \tag{10}$$

where the left-hand side includes the transient and advected energy from neighboring fluid cells $nb$, and the right-hand side captures heat diffusion and the energy source terms: 1) $q'''_{\text{sun}}$, and 2) the internal radiative balance computed via the FV-RTE $q'''_{\text{R}}$.

### 2.3 Hybrid Nearest Neighbor/Barycentric Mapping

To reduce computational cost, a hybrid nearest-neighbor/barycentric direct mapping method can be implemented. In this method, a neighborhood of the $n$ nearest surface/volumetric elements to each $\vec{r}_k$ is identified and the original barycentric direct mapping method is applied exclusively to this neighborhood. The nearest-neighbor algorithm used to identify the neighborhood, or subset of elements eligible for mapping, is defined as:

$$S_{n,i} = \left\{ k = 1,2,\ldots,N_{\text{rays}} \,\middle|\, d_{i,k} \le d_{n/N,k} \right\} \tag{11}$$

where $d_{n/N,k}$ is the size of the neighborhood of $n/N$th percentile nearest elements, defined from distances $d_{i,k} = \left|\left|\vec{r}_k - \vec{r}_{C_i}\right|\right|_2^{1/2}$ calculated between the $\vec{r}_k$ and cell centroids $\vec{r}_{C_i}$. For a sufficiently large neighborhood, the original and hybrid methods produce identical mapping results.

While an exclusively nearest-neighbor direct mapping would be computationally simpler than a barycentric or hybrid method, it could amplify discretization error and introduce instabilities by erroneously mapping rays to neighboring cells. This scenario is demonstrated in Figure 2 for the $\vec{r}_k$within $C_i$: since $d_{i+1} < d_i$, nearest-neighbor direct mapping would map the $\vec{r}_k$ to the prism-shaped cell despite the $\vec{r}_k$ falling within $C_i$. Such errors are more likely to occur for meshes with high skew and large, abrupt element size changes, biasing $\vec{r}_k$ toward nearby small cells. Therefore, the hybrid barycentric direct mapping hybrid method is suggested.

A flow chart detailing the algorithms for direct surface and volumetric mapping from the MCRT to CFD modeling domains is depicted in Figure 3a and b, respectively.

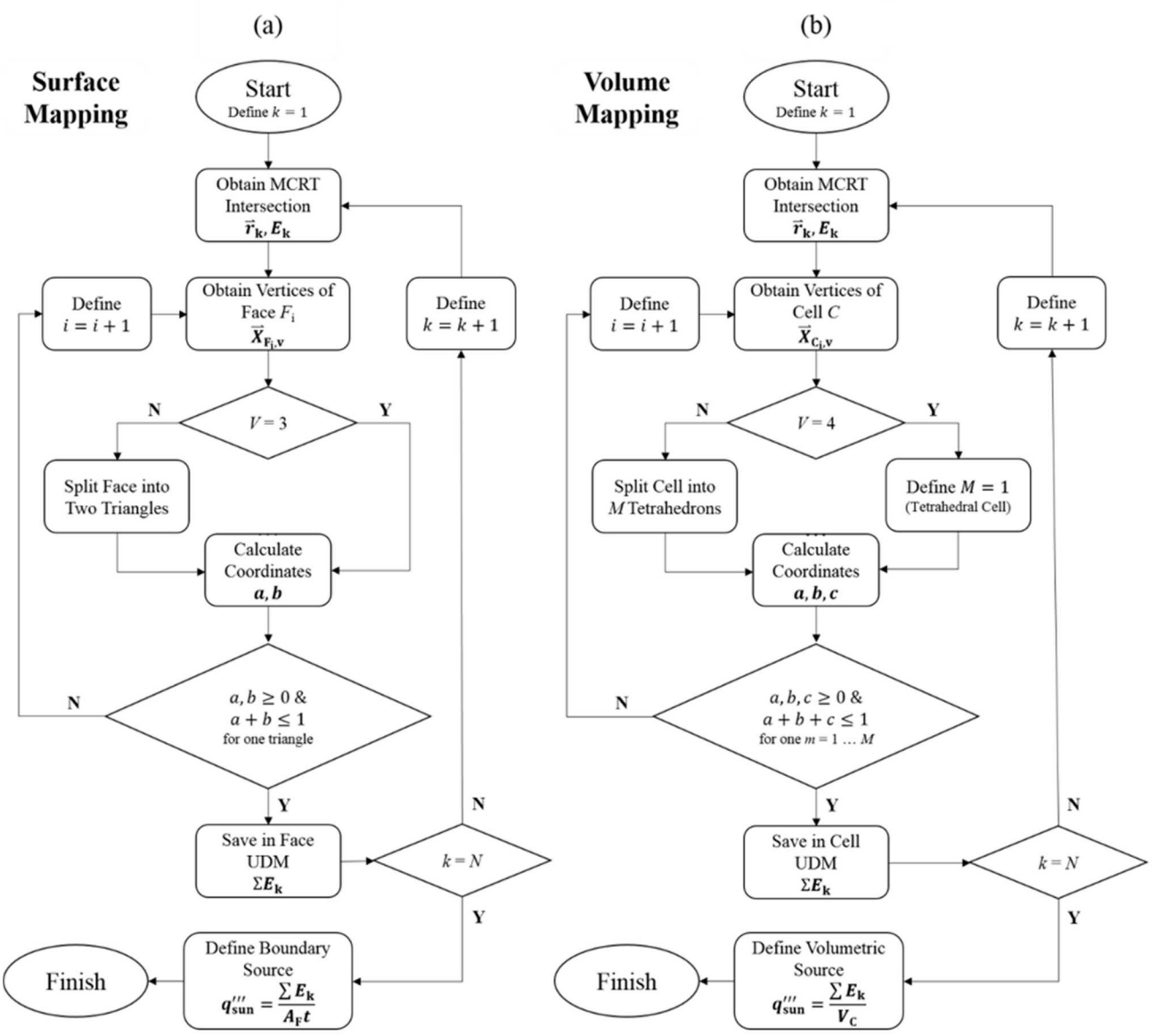


**Figure 3**. Flow charts for mapping of spatially-absorbed, incident irradiation for (a) surface and (b) volume geometries between Monte Carlo ray tracing and computational fluid dynamics modeling domains.

### 2.4 Computational Models

Validation of energy conservation and spatial preservation by the method was performed for the Solar Thermochemical Inclined Granular-Flow Reactor (STInGR). STInGR was designed for 5 $kW_{th}$ scale reduction of redox-active metal oxides directly heated by a HFSS [11]. The combined HFSS-STInGR system, shown in Figure 4 with the relevant components of each system labeled, was modeled using an overlapping scheme. The 142 mm diameter, 5 mm thick quartz window was modeled as a specularly reflecting, non-scattering, participating medium [22]. The empty cavity and conical frustum were modeled as diffusely reflecting alumina surfaces.

The radiative input was modeled using a MCRT of a HFSS comprised of seven Xe arc lamps mounted in truncated ellipsoidal reflectors and aligned to a common focal point [31]. The MCRT was extended to include the semitransparent quartz window and the surfaces comprising the STInGR aperture and internal cavity. The aperture of STInGR was aligned to the HFSS focal plane in the MCRT domain. Emitted rays were assumed to be within the solar spectrum. The MCRT produced $10^6$ rays for each lamp and predicted 8.77 $kW_{th}$ of radiation absorption by the STInGR surfaces and window. The ray intersections from the MCRT were mapped to a 3D mesh produced in ANSYS Mesh for CFD models in ANSYS Fluent. The mesh consisted of 59209 unstructured triangular and quadrilateral face elements and 617 unstructured tetrahedral, hexahedral, or prismatic volumetric elements. The mesh of the STInGR cavity inclined slope was controlled to a uniform grid, such that it was in-effect structured.

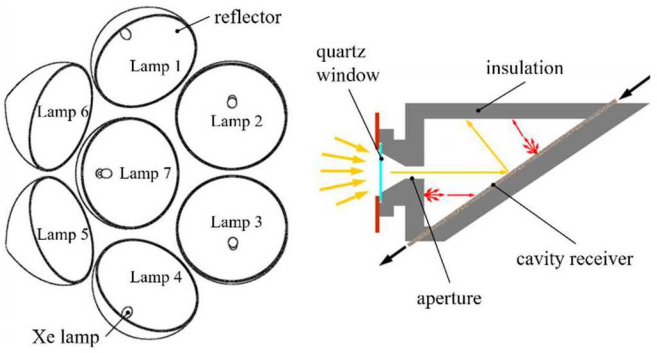


**Figure 4.** Schematic of the high-flux solar simulator with seven Xe arc lamps mounted in truncated ellipsoidal reflectors, with the solar thermochemical inclined granular-flow reactor positioned at the reflector focal point.

Three case studies were performed to investigate preservation of spatial variation and energy conservation for direct mapping for three STInGR surfaces: the inclined slope, ceiling, and conical frustum, labeled as surfaces 1, 2, and 3 in Figure 6, respectively. Structured/unstructured meshes and flat/curved surfaces were represented among the studies. The direct mapping method was compared to the profile interpolation process in ANSYS Fluent. For surface 1, the CFD mesh was structured, so direct mapping could produce identical results to interpolation for an equivalent MCRT grid. For surface 2, the CFD mesh was unstructured, so direct mapping could provide equal or better preservation of spatial variation and energy conservation. For surface 3, the CFD mesh was unstructured, the surface geometry complex (conical), and the irradiation gradients high due to proximity to the HFSS focal point. For this case, binning, interpolation, and mesh resolution deficiencies could produce significant energy losses.

For the profile interpolation process, ANSYS Fluent requires tabular irradiation profiles, *i.e.* lists of fluxes at specified surface coordinates, which are interpolated to the CFD mesh in a nearest-neighbor manner. To obtain the irradiation profiles, the MCRT surface $\vec{r}_k$ were binned to structured grids in MATLAB [10]. Wireframes of the grids used to bin the $\vec{r}_k$ are shown in Figure 5, for (a) the incline slope, (b) the ceiling, and (c) the conical frustum. The grid resolutions were controlled to produce similar numbers of elements as in the corresponding CFD surface meshes. For the direct mapping method, no binning was required and the $\vec{r}_k$ were directly input to the CFD mesh using the mapping algorithm.

To quantitatively compare the energy conservation of both methods, the total energy loss from the MCRT grid to the CFD mesh sources was calculated as:

$$P = \left| \left( \sum_i A_i q''_{\text{sun,i}} \right)_{\text{CFD}} - \left( \sum_j A_j q''_{\text{sun,j}} \right)_{\text{MCRT}} \right| \tag{12}$$

where $i$ and $j$ are the indices of CFD mesh and MCRT grid elements, respectively.

To quantitatively compare the spatial accuracy of the methods, the CFD mesh boundary source fluxes from 1) the profile interpolation process in ANSYS Fluent and 2) the direct mapping method were both linearly interpolated back to the structured surface grids used in the profile binning. These were quantitatively compared to the fluxes from the originally binned $\vec{r}_k$ via the sum of square errors, calculated as:

$$SSE = \sum_j \left( q''_{\text{sun,j}}\big|_{\text{CFD}} - q''_{\text{sun,j}}\big|_{\text{MCRT}} \right)^2 \tag{13}$$

For complete energy conservation and preservation of spatial variation, $P \to 0$ and $SSE \to 0$, respectively.

A final case study was performed on the solar thermochemical reactor quartz window to demonstrate the application of the direct volumetric mapping algorithm to participating media. As profile interpolation for volumetric sources was not supported in ANSYS Fluent v19.0, the case study was instead compared to a simple, independent nearest-neighbor sorting algorithm as described in Section 2.2.

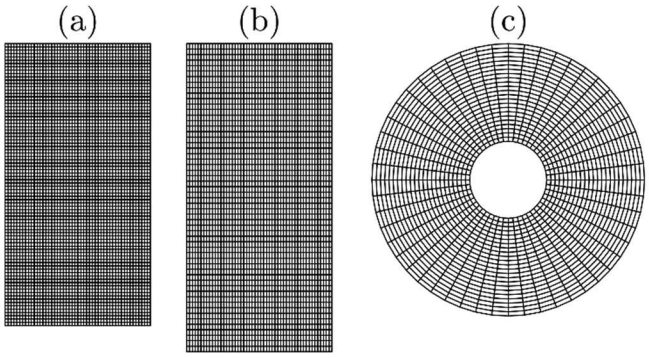


**Figure 5.** The grids used to bin results from a Monte Carlo ray tracing model to absorbed irradiation profiles, applied as boundary sources in ANSYS Fluent, for the reactor (a) inclined slope, (b) cavity ceiling, and (c) conical frustum.

## 3. RESULTS AND DISCUSSION

An isometric view of the solar reactor inclined slope (1), walls including ceiling (2), and conical aperture (3) are given in Figure 6. Each CFD mesh element is colored according to the absorbed irradiation, which was applied in ANSYS Fluent as a boundary source via the direct mapping method.

In Figure 6, localized regions of highly concentrated absorbed irradiation from individual lamps are clear along the internal cavity and external front face surfaces. The localization was particularly evident along the inclined slope and would not have been captured by a uniform or spatially-averaged heat flux profile. The total energy mapped to the reactor surfaces was $\sum_i (q''_{\text{sun,i}} A_i) = 8.29$ kW$_{\text{th}}$. The total energy mapped to the quartz window was $\sum_i (q'''_{\text{sun,i}} V_i) = 0.48$ kW$_{\text{th}}$. The total 8.77 kW$_{\text{th}}$ mapped to the CFD mesh in ANSYS Fluent was equal to the 8.77 kW$_{\text{th}}$ from the MCRT, confirming energy conservation between the MCRT and CFD.

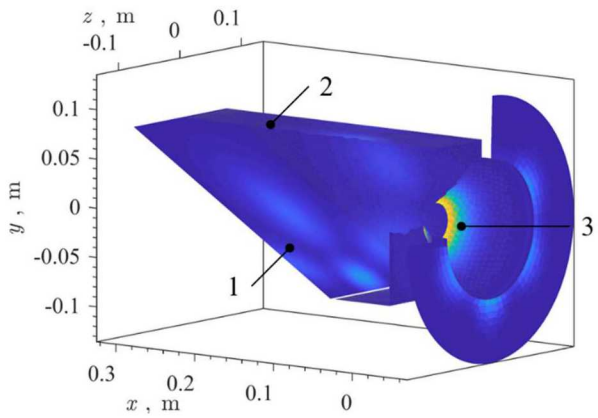


**Figure 6.** Isometric view of the solar reactor, including the aperture exterior and cavity interior, with the magnitude of mapped absorbed irradiation from a seven-lamp high flux solar simulator using the direct mapping method, between 0 (dark blue) and 800 kW·m$^{-2}$ (yellow).

### 3.1 Surface Case Study I: Inclined Slope

The first case study is a scenario in which the direct mapping method performs identically to previous methods. Normal views of the STInGR cavity inclined slope are given in Figure 7, with the mesh elements colored by the total absorbed irradiation. The slope was discretized as a structured, uniform mesh in the CFD domain with 4250 quadrilateral elements aligned with the MCRT grid. Four local regions of absorbed irradiation were captured in Figure 7a-c from individual HFSS lamps. Peak fluxes up to 300 kW·m$^{-2}$ and a total absorbed power of 1.91 kW$_{th}$ were predicted.

In Figure 7a and b, nearly identical distributions of absorbed irradiation for the two methods were observed due to effectively exact alignment between MCRT grid and CFD mesh. Both methods achieved complete energy conservation ($P$ = 0 kW$_{th}$) and high spatial preservation, with $SSE_{interp}$ = 0.003 and $SSE_{map}$ = 0.711, respectively. The spatial errors resulted solely due to differences in numerical precision between C and MATLAB, as no interpolation between modeling domains was required. Therefore, for structured meshes that aligned exactly to the binned MCRT grid, the direct mapping method is identical to the interpolated profile method.

### 3.2 Surface Case Study II: Reactor Ceiling

The second case study is a scenario in which the direct mapping method performs equivalently to or better than previous methods. Normal views of the meshed STInGR ceiling are given in Figure 8, with the mesh elements colored by the total absorbed irradiation. The ceiling was discretized as an unstructured, non-uniform mesh in the CFD domain with 2864 elements. Three local regions of absorbed irradiation were captured in Figure 8a and b from individual HFSS lamps. Peak fluxes of 150 kW·m$^{-2}$ and a total absorbed power of 0.97 kW$_{th}$ were predicted.

In Figure 8a, slight degradation in spatial accuracy using the profile interpolation method is evident, particularly for $F_i$ with absorbed irradiation of 50–100 kW·m$^{-2}$. The elliptical profile was better preserved by direct mapping, as observed in Figure 8b. Spatial accuracy and energy conservation were

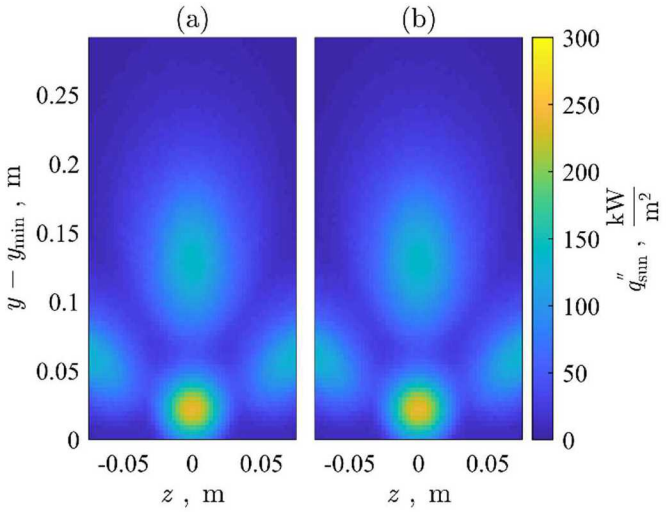


**Figure 7.** Absorbed irradiation on the inclined slope, mapped from ray tracing of a seven-lamp solar simulator using: (a) the interpolated profile method, (b) the direct mapping method.

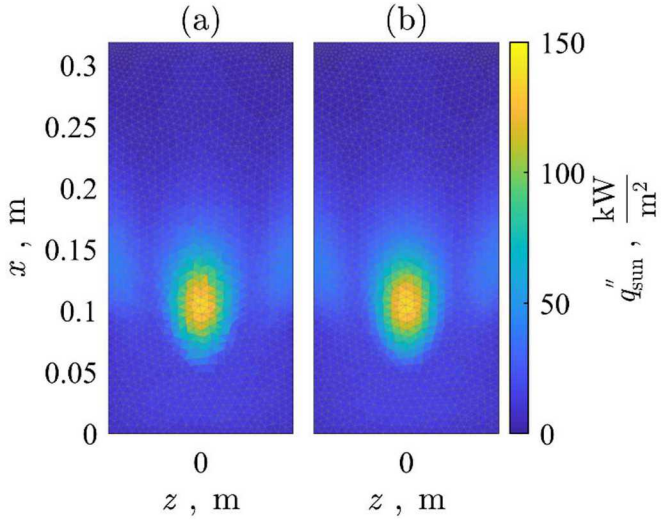


**Figure 8.** Absorbed irradiation on the cavity ceiling, mapped from ray tracing of a seven-lamp solar simulator using: (a) the interpolated profile method, (b) the direct mapping method.

achieved, respectively, to $SSE_{map}$ = 5.8 x10$^3$ < $SSE_{interp}$ = 7.5x10$^3$ and $P_{map}$ = 0 < $P_{interp}$ = 0.004 kW$_{th}$. While both methods approximately preserved the spatial profile shape without significant energy losses, the direct mapping method achieved better spatial accuracy (lower *SSE*) and complete energy conservation.

### 3.3 Surface Case Study III: Reactor Aperture

The third case study demonstrated a scenario in which the direct mapping method not only preserves spatial accuracy better than previous methods, but is even critical to prevent significant energy losses. A normal view of the STInGR aperture, a conical frustum shape, is given in Figure 9, with the mesh elements

colored by the magnitude of absorbed irradiation. An inset in the bottom right of (b) is presented to show the spatial variation. The frustum was discretized as an unstructured, non-uniform mesh in the CFD modeling domain with 1182 elements. Radially-uniform profiles are present in Figure 9 due a 2.3 $kW_{th}$ spillage of concentrated radiation from the HFSS around the aperture.

The direct mapping method qualitatively preserved the spatial profile shape better than profile interpolation. However, the approximation of the conical surface as planar faces in the CFD mesh produced a mismatch between the locations of the MCRT grid and CFD mesh elements and between the total surface areas in the MCRT grid (0.022 $m^2$) and CFD mesh (0.020 $m^2$). This mismatch prevented a meaningful quantitative *SSE* comparison before and after coupling.

A significantly smaller magnitude of absorbed irradiation was observed in Figure 9a compared to Figure 9b due to the highly concentrated irradiation in the focal plane. High flux gradients near the aperture led to underestimation during interpolation, producing a peak $q''_{sun} = 15 \ll 800$ kW·m$^{-2}$, as shown in the inset. Energy conservation analysis resulted in $P_{map} = 0 < P_{interp} = 2.25$ $kW_{th}$, indicating that profile interpolation may introduce large errors in energy conservation depending on: 1) the irradiation gradient and 2) MCRT grid/CFD mesh resolutions. Direct mapping, however, was demonstrated as robust even for sharp irradiation profiles and/or coarse meshes.

Comparison of mapping methods for the three studies pictured in Figure 7-9 demonstrated the inherent energy conservative nature of the direct mapping method, with spatial accuracy dependent upon discretization accuracy of the modeled geometry. The method was also demonstrated to be independent of the non-trivial process of matching gridded MCRT and meshed CFD modeling domains. Direct mapping achieved equivalent accuracy to the interpolated profile method for aligned MCRT grids/CFD meshes and improved accuracy for misaligned MCRT grids/CFD meshes.

### 3.4 Volumetric Case Study: Quartz Window

A final case study was performed to demonstrate the direct mapping method for participating media and to demonstrate improved performance over the independent nearest-neighbor algorithm. A view of the STInGR window depicting the unstructured CFD mesh cell centroids is given in Figure 10a and b. Each cell is colored according to the total volumetrically absorbed radiation, which was applied as a volumetric heat source in ANSYS Fluent using (a) nearest neighbor direct mapping and (b) barycentric direct mapping, respectively.

Using both algorithms, the profile of the seven-lamp HFSS, roughly symmetric about (0,0), was visible. In Figure 10a, however, localized $C_i$ of high or low $q'''_{sun}$ not present in (b) are evident. The differences were the result of ray misappropriation by the nearest neighbor algorithm for neighboring cells with significant volume differences. The most prominent example of ray misappropriation in Figure 10a occurred at the cell centroid near (0.01,0), producing a local hotspot of $q'''_{sun} \approx 1.9 \times 10^4$ kW·m$^{-2}$. The meshed element and centroid are pictured in greater detail in Figure 2 as element $C_{i+1}$. In Figure 10b, the $q'''_{sun}$ profile

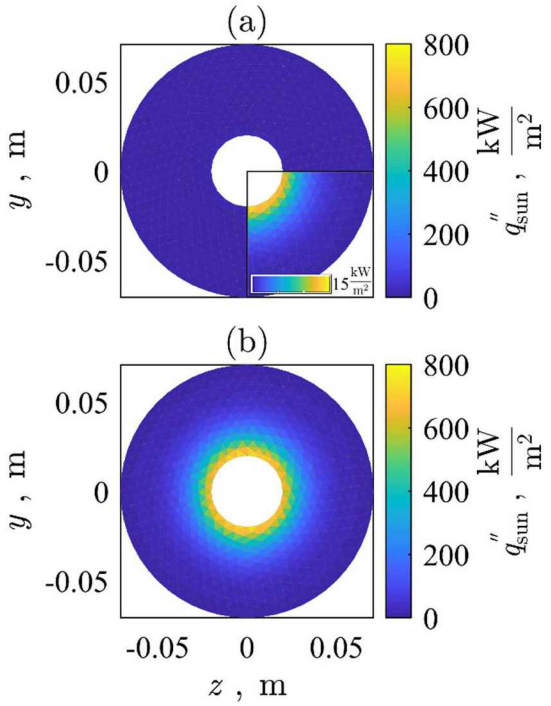


**Figure 9.** Irradiation absorbed on the conical frustum, mapped from ray tracing of a seven-lamp solar simulator via: (a) the interpolated profile method, (b) the direct mapping method; a quarter inset on (a) emphasizes the peak flux of only 15 kW·m$^{-2}$ via profile interpolation.

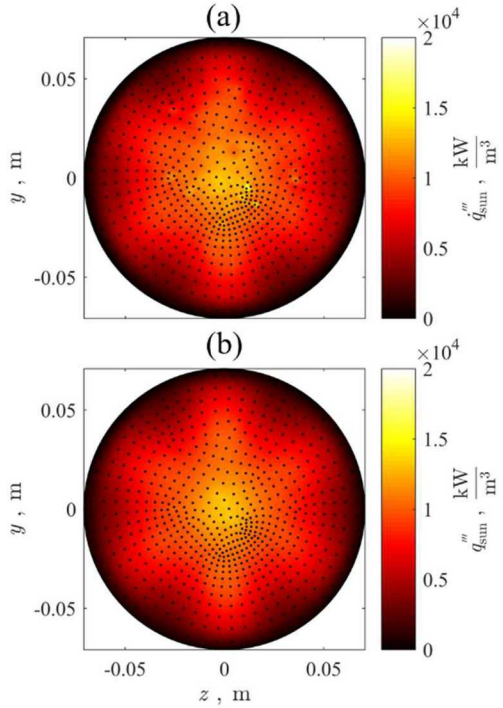


**Figure 10.** Volumetrically absorbed radiation within the reactor quartz window with overlaid volumetric cell centroids, mapped from a ray tracing of a seven-lamp solar simulator using: (a) nearest-neighbor and (b) direct mapping methods.

was smoother as a result of the barycentric mapping algorithm, indicating improved mapping between the MCRT and CFD modeling domains.

Based upon the methodology and observations from the case studies, the advantages and disadvantages of the method are summarized in the following subsections. Note that all disadvantages are also true for other overlapping modeling domain schemes. The disadvantages may also be reasonably mitigated in most scenarios.

### 3.5 Advantages

1) The method is energy conservative between the MCRT and CFD modeling domains.
2) The method is spatially accurate to within the MCRT and CFD discretization accuracies.
3) The method is compatible with structured and unstructured meshes of arbitrary polygonal or polyhedral construction, for two and three dimensions.
4) The method uses an algorithm that is programmatically simple and may be applied using an external code or directly within ANSYS Fluent via UDFs.
5) The method requires that the MCRT run only once for a given geometry and radiative conditions, even when performing CFD mesh refinement.

### 3.6 Disadvantages

1) Transient mapping is cumbersome using the method. Such cases occur for overlapping schemes with participating media in the band(s) of the radiative solar input. Non-overlapping domains or a single computational domain may be more appropriate for media with highly temperature-dependent absorption, transmission, reflection, or scattering.
2) Systematic errors in the absorbed heat flux distribution are introduced by approximating curved geometries from the MCRT model with polygonal elements in the CFD model.
3) The method utilizes boundary sources for surface elements. Boundary sources in ANSYS Fluent require definition of a boundary region of nonzero thickness which introduces additional conductive resistance at the interface [3]. The additional resistance becomes negligible for a sufficiently thin boundary with sufficiently high conductivity.

## 4. CONCLUSION

A method for mapping radiative inputs from ray tracing simulations to computational heat transfer models was presented. The method if preferable to previous documented attempts, as it may be rapidly implemented, yet maintains energy conservation and spatial patterns between the two modeling domains to within mesh precision.

The direct mapping method was implemented for a model of a windowed, solar thermochemical reactor with input radiation from a high flux solar simulator. The method captured local hotspots from individual lamps without losses in net energy absorption due to direct mapping from the Monte Carlo ray tracing to the computational fluid dynamics mesh. The method was demonstrated to preserve spatial variation and to maintain energy conservation equivalent to or better than previous methods, for various complex geometries and mesh types. The direct mapping method is a useful tool for developing solar infrastructure, as it enables the accurate modeling of highly directional/spatial concentrated solar inputs.

## ACKNOWLEDGMENTS

This material is based upon work supported by the National Science Foundation Graduate Research Fellowship under Grant No. DGE-1650044. Any opinions, findings, and conclusions or recommendations expressed in this material are those of the author(s) and do not necessarily reflect the views of the National Science Foundation. This material is also based upon work supported by the U.S. Department of Energy SunShot initiative under Award No. DE-FOA-0000805-1541.

This publication derives from work while all authors were affiliated with the Georgia Tech Solar Fuels and Technology Lab (Peter G. Loutzenhiser). At publication time, H. Evan Bush is a Postdoctoral Researcher at Sandia National Labs in Concentrating Solar Technologies (hebush@sandia.gov). Sandia National Laboratories is a multimission laboratory managed and operated by National Technology & Engineering Solutions of Sandia, LLC, a wholly owned subsidiary of Honeywell International Inc., for the U.S. Department of Energy's National Nuclear Security Administration under contract DE-NA0003525. At publication time, Andrew Schrader is an Assistant Professor at the University of Dayton in Mechanical and Aerospace Engineering (aschrader1@udayton.edu).

## REFERENCES

[1] Patankar, S., 1980, Numerical heat transfer and fluid flow, CRC press.

[2] Anderson, D., Tannehill, J., and Pletcher, R., "Computational Fluid Mechanics and Heat Transfer, series in computational methods in mechanics and thermal sciences second edition," Taylor and Francis.

[3] 2013, "ANSYS Fluent," ANSYS, Inc., Canonsburg, PA.

[4] Modest, M. F., 2013, Radiative Heat Transfer, Academic Press, Oxford, UK.

[5] ANSYS, 2017, "ANSYS Fluent," ANSYS, Inc., Canonsburg, PA.

[6] Mecit, A. M. M., F., 2014, "A Comparison Between the Monte Carlo Ray Trace and the FLUENT Discrete Ordinates Methods for Treating Solar Input to a Particle Receiver," ASME 2014 8th International Conference on Energy Sustainability collocated with the ASME 2014 12th International Conference on Fuel Cell Science, Engineering and Technology, Volume 1: Combined Energy Cycles, CHP, CCHP, and Smart Grids; Concentrating Solar Power, Solar Thermochemistry and Thermal Energy Storage; Geothermal, Ocean, and Emerging Energy Technologies; Hydrogen Energy Technologies; Low/Zero Emission Power Plants and Carbon Sequestration; Photovoltaics; Wind Energy Systems and Technologies, p. V001T002A013.

[7] Craig, K. J., Moghimi, M. A., Rungasamy, J., Marsberg, J., and Meyer, P., 2016, "Finite-volume ray tracing using Computational Fluid Dynamics in linear focus CSP applications," Appl. Energ., 183, pp. 241-256.
[8] Wang, F., Tan, J., Yong, S., Tan, H., and Chu, S., 2014, "Thermal performance analyses of porous media solar receiver with different irradiative transfer models," International Journal of Heat and Mass Transfer, 78, pp. 7-16.
[9] Khalsa, S. S. S., and Ho, C. K., 2011, "Radiation Boundary Conditions for Computational Fluid Dynamics Models of High-Temperature Cavity Receivers," Journal of Solar Energy Engineering, 133(3).
[10] Bush, H. E., Schlichting, K.-P., Gill, R. J., Jeter, S. M., and Loutzenhiser, P. G., 2017, "Design and Characterization of a Novel Upward Flow Reactor for the Study of High-Temperature Thermal Reduction for Solar-Driven Processes," Journal of Solar Energy Engineering, 139(5), pp. 051004-051004-051011.
[11] Schrader, A. J., De Dominicis, G., Schieber, G. L., and Loutzenhiser, P. G., 2017, "Solar electricity via an Air Brayton cycle with an integrated two-step thermochemical cycle for heat storage based on Co3O4/CoO redox reactions III: Solar thermochemical reactor design and modeling," Sol. Energy, 150, pp. 584-595.
[12] Qiu, Y., He, Y.-L., Wu, M., and Zheng, Z.-J., 2016, "A comprehensive model for opitcal and thermal characterization of a linear Fresnel solar reflector with a trapezoidal cavity receiver," Renewable Energy, 97, pp. 129-144.
[13] Qiu, Y., He, Y.-L., Cheng, Z.-D., and Wang, K., 2015, "Study on optical and thermal perforamance of a linear Fresnel solar reflector using molten salt as HTF with MCRT and FVM methods," Appl. Energ., 146, pp. 162-173.
[14] He, Y.-L., Xiao, J., Cheng, Z.-D., and Tao, Y.-B., 2010, "A MCRT and FVM coupled simulation method for energy conversion process in parabolic trough solar collector," Renewable Energy, 36, pp. 976-985.
[15] Lapp, J., Davidson, J. H., and Lipiński, W., 2013, "Heat Transfer Analysis of a Solid-Solid Heat Recuperation System for Solar-Driven Nonstoichiometric Redox Cycles," Journal of Solar Energy Engineering, 135(3), pp. 031004-031004-031011.
[16] Koepf, E., Advani, S. G., Steinfeld, A., and Prasad, A. K., 2012, "A novel beam-down, gravity-fed, solar thermochemical receiver/reactor for direct solid particle decomposition: Design, modeling, and experimentation," International Journal of Hydrogen Energy, 37(22), pp. 16871-16887.
[17] Alonso, E., and Romero, M., 2015, "A directly irradiated solar reactor for kinetic analysis of non-volatile metal oxides reductions," International Journal of Energy Research, 39(9), pp. 1217-1228.
[18] Bush, H. E., 2019, "Development and characterization of novel reduction-oxidation active materials for two-step solar thermochemical cycles,"Ph.D. Dissertation, Georgia Institute of Technology, Atlanta, Georgia, USA.
[19] Dai, G.-L., Xia, X.-L., and Hou, G.-F., 2014, "Transmission performances of solar windows exposed to concentrated sunlight," Solar Energy, 103, pp. 125-133.
[20] Yong, S., Fu-Qiang, W., Xin-Lin, X., He-Ping, T., and Ying-Chun, L., 2011, "Radiative properties of a solar cavity receiver/reactor with quartz window," International journal of hydrogen energy, 36(19), pp. 12148-12158.
[21] Mecit, A. M., and Miller, F., "Optical analysis of a window for solar receivers using the Monte Carlo ray trace method," Proc. ASME 2013 7th International Conference on Energy Sustainability collocated with the ASME 2013 Heat Transfer Summer Conference and the ASME 2013 11th International Conference on Fuel Cell Science, Engineering and Technology, American Society of Mechanical Engineers, pp. V001T011A003-V001T011A003.
[22] Müller, R., and Steinfeld, A., 2007, "Band-approximated radiative heat transfer analysis of a solar chemical reactor for the thermal dissociation of zinc oxide," Sol. Energy, 81(10), pp. 1285-1294.
[23] Cunsolo, S., Oliviero, M., Harris, W. M., Andreozzi, A., Bianco, N., Chiu, W. K. S., and Naso, V., 2015, "Monte Carlo determination of radiative properties of metal foams: Comparison between idealized and real cell structures," International Journal of Thermal Sciences, 87, pp. 94-102.
[24] Wei, G., Huang, P., Xu, C., Chen, L., Ju, X., and Du, X., 2017, "Experimental study on the radiative properties of open-cell porous ceramics," Solar Energy, 149, pp. 13-19.
[25] Cui, F. Q., He, Y. L., Cheng, Z. D., Li, D., and Tao, Y. B., 2012, "Numerical simulations of the solar transmission process for a pressurized volumetric receiver," Energy, 46(1), pp. 618-628.
[26] Li, Y., Xia, X.-L., Ai, Q., Sun, C., and Tan, H.-P., 2018, "Pore-level determination of spectral reflection behaviors of high-porosity metal foam sheets," Infrared Physics & Technology, 89, pp. 77-87.
[27] Akolkar, A., and Petrasch, J., 2011, "Tomography based pore-level optimization of radiative transfer in porous media," International Journal of Heat and Mass Transfer, 54(23), pp. 4775-4783.
[28] Marti, J., Roesle, M., and Steinfeld, A., 2014, "Combined Experimental-Numerical Approach to Determine Radiation Properties of Particle Suspensions," Journal of Heat Transfer, 136(9), p. 092701.
[29] Marti, J., Roesle, M., and Steinfeld, A., 2014, "Experimental determination of the radiative properties of particle suspensions for high-temperature solar receiver applications," Heat Transfer Engineering, 35(3), pp. 272-280.
[30] Tien, C. L., 1988, "Thermal Radiation in Packed and Fluidized Beds," Journal of Heat Transfer, 110(4b), pp. 1230-1242.
[31] Gill, R., Bush, H. E., Haueter, P., and Loutzenhiser, P., 2015, "Characterization of a 6 kW high-flux solar simulator with an array of xenon arc lamps capable of concentrations of nearly 5000 suns," Review of Scientific Instruments, 86(12), p. 8.

 